JGR Solid Earth

RESEARCH ARTICLE
10.1029/2020JB020411

Stress Promotion of the 1958 M_w~7.8 Fairweather Fault Earthquake and Others in Southeast Alaska by Glacial Isostatic Adjustment and Inter-earthquake Stress Transfer

Chris Rollins[1,2,3], **Jeffrey T. Freymueller**[1,2], **and Jeanne M. Sauber**[4]

[1]Department of Geosciences, Geophysical Institute, University of Alaska Fairbanks, Fairbanks, AK, USA, [2]Department of Earth and Environmental Sciences, Michigan State University, East Lansing, MI, USA, [3]School of Earth and Environment, University of Leeds, Leeds, UK, [4]Lab for Geodesy and Geophysics, NASA Goddard Space Flight Center, Greenbelt, MD, USA

Abstract We assess how recent glacial isostatic adjustment (GIA) and inter-earthquake stress transfer modulated the state of stress on major faults in Southeast Alaska, and how these effects may have influenced recent large and moderate earthquakes. The Glacier Bay Icefield has lost >3,000 km^3 of ice since ca. 1770, with ice thinning up to 1.5 km, and the rest of southeast Alaska has been deglaciating since ca. 1900. The resulting GIA response in the solid earth produces present-day surface uplift rates of up to ~4 cm/yr, among the fastest on Earth. This rapid deformation occurs directly alongside and atop the Fairweather Fault, which accommodates 4–5 cm/yr of right-lateral motion through slip in frequent large earthquakes, recently including a M_w~7.8 earthquake in 1958. We find that the 1958 earthquake nucleated very close to the location of maximum GIA-induced Coulomb stress increase on the Fairweather Fault between 1770 and 1958 (estimated at ~0.2–0.6 MPa), on the only section of fault where GIA-induced stress changes had involved both right-lateral shearing and unclamping. The September 10, 1899 M_w~8.1 Yakutat Bay earthquake also promoted failure on at least the northwest part of the eventual 1958 rupture. In turn, the 1899 and 1958 earthquakes and GIA promoted failure along the St. Elias compressional margin, the site of a M_w~7.4 event in 1979. While rapid tectonic loading is very likely the main driver of earthquakes in southeast Alaska, we estimate that 23 of 30 instrumentally constrained $M_w \geq 5.0$ earthquakes in this region were also promoted by post-1770 GIA.

Key Points:

- The 1958 Fairweather Fault earthquake nucleated very close to the maximum post-1770-GIA-induced Coulomb stress increase on the fault
- The September 10, 1899 M_w~8.1 earthquake promoted failure at the northwest end of the 1958 rupture, and on thrust faults of the St. Elias margin
- Post-1770 GIA likely promoted failure in 23 of the 30 $M_w \geq 5.0$ recorded earthquakes in southeast Alaska since 1920

Supporting Information:

Supporting Information may be found in the online version of this article.

Correspondence to:

C. Rollins,
j.c.rollins@leeds.ac.uk

Citation:

Rollins, C., Freymueller, J. T., & Sauber, J. M. (2021). Stress promotion of the 1958 M_w~7.8 Fairweather Fault earthquake and others in southeast Alaska by glacial isostatic adjustment and inter-earthquake stress transfer. *Journal of Geophysical Research: Solid Earth*, *126*, e2020JB020411. https://doi.org/10.1029/2020JB020411

Received 15 JUN 2020
Accepted 5 DEC 2020

© 2020. The Authors.
This is an open access article under the terms of the Creative Commons Attribution License, which permits use, distribution and reproduction in any medium, provided the original work is properly cited.

1. Introduction

1.1. Background and Motivation

Southeast Alaska provides a unique opportunity to study the influence of glacial isostatic adjustment (GIA) on fault stress and earthquake activity. Since ca. 1770 AD, the Glacier Bay Icefield alone has lost >3,000 km^3 of ice, with ice thinning up to 1.5 km (Figure 1a, grayscale squares). (High-resolution versions of the figures from the main text of this article can be found in the Supporting Information as Figures S20–S29.) Deglaciation began throughout the rest of southeast Alaska ca. 1900 and accelerated toward the end of the 20th century (Larsen et al., 2004, 2005). This past ice loss induces a prolonged viscoelastic response in the solid earth, while continuing ice loss induces an (effectively instantaneous) elastic response. In southeast Alaska, these two responses combine to produce present-day surface uplift rates of up to ~4 cm/yr, among the fastest on Earth, coupled with several mm/yr of horizontal motion (J. L. Elliott et al., 2010; Hu & Freymueller, 2019; Larsen et al., 2004, 2005). The fastest uplift is centered on the area of greatest past ice loss in Glacier Bay (Figure 1a, small colored circles).

Somewhat uniquely to Southeast Alaska, this rapid GIA is superimposed on rapid tectonic deformation that includes both strike-slip and thrust faults (Section 1.2). These faults frequently rupture in large earthquakes, recently including two M_w~8.1 events in 1899, a M_w~7.8 strike-slip earthquake in 1958, a M_w~7.4 oblique-thrust event in 1979, and many smaller earthquakes throughout the 20th century (Figure 1a). This juxtaposition provides an opportunity to study how GIA may impact earthquake behavior, and to do so in a setting that includes strike-slip tectonics, a regime in which this effect is rarely studied (Section 3.1). In the St. Elias thrust margin, site of the 1979 M_w~7.4 event and just northwest of the 1958 M_w~7.8 event,

Printed by [Nasa Goddard Space Flight - 156.068.119.100 - /doi/epdf/10.1029/2020JB020411] at [16/08/2021].

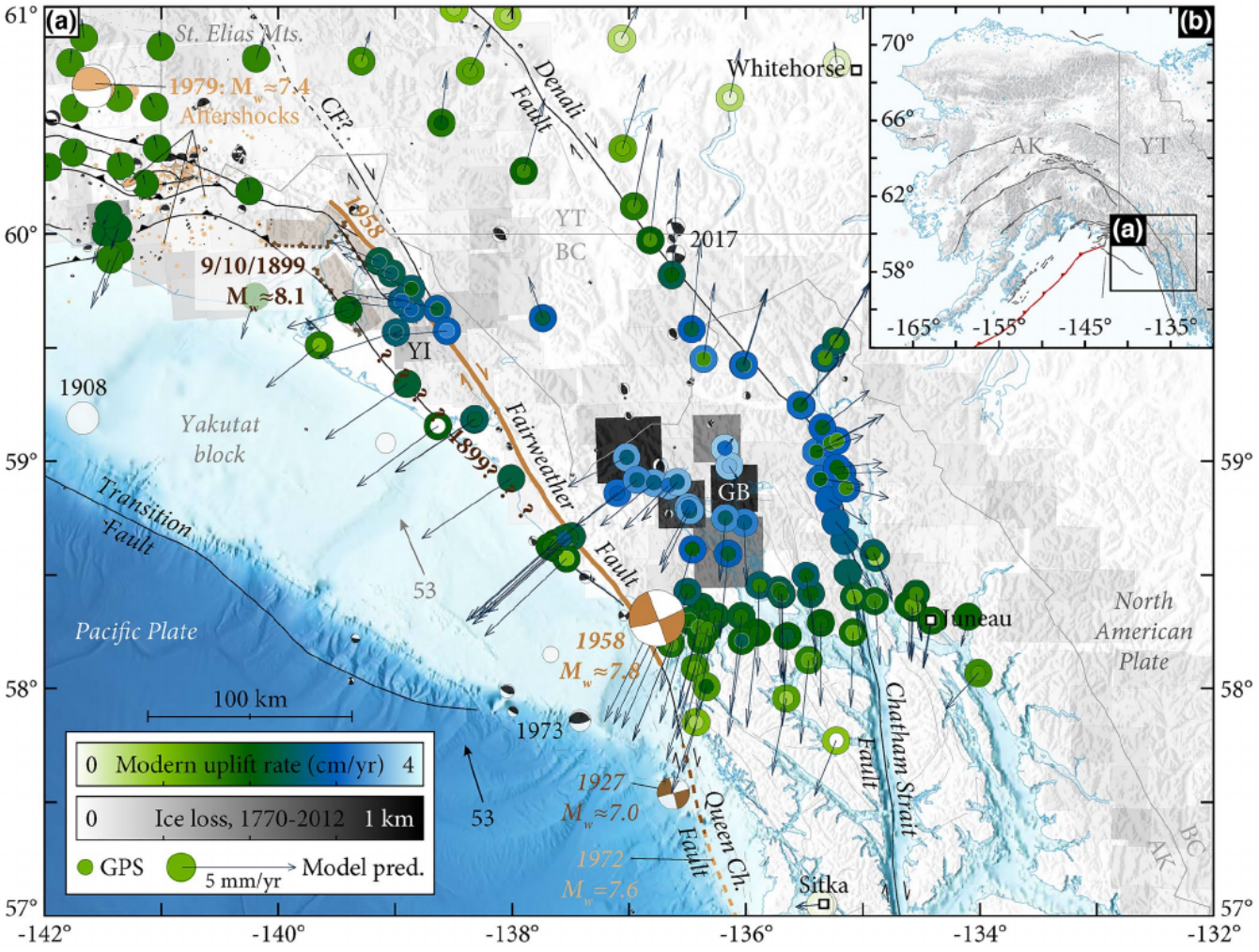


Figure 1. (a) Tectonics, glacial isostatic adjustment (GIA), and recent earthquakes in southeast Alaska. Small colored circles: GPS-derived uplift rates from Hu and Freymueller (2019) (HF19) over 1992–2003 (white edges) and 2003–2012 (black edges). Grayscale squares: cumulative 1770–2012 ice loss in HF19 GIA model. Large colored circles and dark blue arrows: HF19-R model predictions of GIA-related vertical and horizontal motions (Section 4), averaged over 1992–2012. Earthquakes are described in Section 4 and supporting information Text S4. The September 4, 1899 M_w~8.1 earthquake occurred somewhere west of the September 10, 1899 earthquake near the coast, likely off the figure (Doser, 2006). Black fault traces are from Alaska Division of Geological and Geophysical Surveys Quaternary Fault and Fold (QFF) database (R. D. Koehler, 2013); faint gray fault traces are from Plafker et al. (1994); Connector Fault (cf.) is described in Section 4. Black vector: motion of Pacific Plate relative to North America from DeMets et al. (2010). Gray vector: motion of Yakutat block relative to North America from Elliott et al. (2010) Euler pole. GB: Glacier Bay. YI: Yakutat Icefield. (b) Location of study region. Red trace: Alaska-Aleutian subduction trench.

Sauber and Molnia (2004) and Sauber and Ruppert (2008) found that seasonal and interannual changes in ice load can influence seismicity rate. Recently, Hu and Freymueller (2019) (hereafter HF19) developed an updated model of post-1770 GIA in southeast Alaska based on 2 decades of geodetic data. In this study, we use variants of the HF19 model to compute the history of GIA-induced stress changes in the region. We also assess the stress changes imparted by the coseismic and postseismic deformation of the 1899 and 1958 earthquakes.

1.2. Tectonic Setting and Recent Earthquakes (Figure 1)

The tectonics and earthquakes of southeast Alaska are driven by larger-scale tectonic interactions between the Pacific and North American plates. Along the coast of northern British Columbia and southeast Alaska, the offshore Pacific Plate moves north-northwest at ~5 cm/yr relative to the North American plate (Figure 1, black arrow) along the right-lateral strike-slip Queen Charlotte Fault (QCF) (e.g., D. S. Brothers et al., 2020;

Printed by [Nasa Goddard Space Flight - 156.068.119.100 - /doi/epdf/10.1029/2020JB020411] at [16/08/2021].

ten Brink et al., 2018). In the northeastern Gulf of Alaska, the Pacific Plate is carrying the ~30-km-thick Yakutat block (Worthington et al., 2012) north-northwestward along the coast of southeast Alaska and wedging it into and beneath southern Alaska. The Yakutat block moves at the same rate as the Pacific Plate, although in a direction ~9° more westerly (Figure 1, gray arrow), and its motion past southeast Alaska is mostly accommodated by the right-lateral Fairweather Fault (hereafter FWF), the northward continuation of the QCF (e.g., Elliott and Freymueller, 2019; Plafker et al., 1978). (The Chatham Strait Fault, which lies to the east and connects to the eastern Denali Fault, is thought to be inactive at present [D. S. Brothers et al., 2018; J. Elliott and Freymueller, 2019; Plafker et al., 1994]) The QCF and FWF therefore dominate the tectonics of southeast Alaska, are often jointly called the Queen Charlotte-Fairweather fault system (hereafter QC-FWF), and frequently rupture in large earthquakes. In 1958, a M_w~7.8 earthquake ruptured most or all of the ~350-km onshore length of the FWF (Doser, 2010; Plafker et al., 1978) and triggered a large rockslide that caused a megatsunami in coastal Lituya Bay (e.g., Miller, 1961). Further south, the QC-FWF ruptured in a M_w~7.0 event in 1927 (Doser & Lomas, 2000), a M_w~7.9 earthquake offshore British Columbia in 1949 (e.g., Lay et al., 2013), a $M_w = 7.6$ shock offshore Sitka, Alaska in 1972 (Schell & Ruff, 1989), and most recently the 2013 $M_w = 7.5$ Craig, Alaska earthquake (Ding et al., 2015). A portion of the QC-FWF near Sitka may have also ruptured in a M_w~7.5 event in 1848 (supporting information Text S1).

On its north side, the Yakutat block is colliding with and subducting beneath southern Alaska at ~4 cm/yr along the St. Elias fold-and-thrust belt (e.g., J. Elliott et al., 2013; J. Sauber et al., 1997). This rapid compression produces both the high topography of the St. Elias Mountains (the highest coastal mountain range on Earth) and abundant seismicity with pervasive thrust mechanisms (Figure 1a). The largest recorded earthquake in the St. Elias, a M_w~7.4 oblique-thrust event in 1979, likely ruptured a subhorizontal decollement at the base of the fold-and-thrust belt (Estabrook et al., 1992) and was followed by a dense aftershock sequence southeast of the epicenter (Figure 1a, beige circles). A M_w~5.9 oblique-normal earthquake in 1920 also suggests some variability in the local stress state (Doser & Lomas, 2000).

The transition between NNW-SSE dextral shear on the FWF and NNW-SSE convergence in the St. Elias occurs in and around Yakutat Bay (e.g., Bruhn et al., 2004). Two M_w~8.1 earthquakes struck this region in September 1899. The first, on September 4, likely occurred west of Yakutat Bay, uplifting a terrace by ~1 m at Cape Yakataga. The second, on September 10, ruptured a set of thrust or oblique-thrust faults around Yakutat Bay and possibly further southeast along the coast (Plafker & Thatcher, 2008; Figure 1a). Southeast of Yakutat Bay, a portion of the FWF's dextral shear may also be transferred onto a postulated Connector Fault (Figure 1a, dashed line) that connects to the Totschunda and Denali faults in interior Alaska (Doser, 2014; J. Elliott & Freymueller, 2019; J. L. Elliott et al., 2010; Kalbas et al., 2008).

These tectonic features are accompanied by several secondary elements. The FWF strikes more westerly than the relative Yakutat-North America motion it accommodates (Figure 1a), resulting in a component of Yakutat-North America convergence. This may be taken up by coastal NW-striking thrust faults that strike parallel or subparallel to the FWF (Bruhn et al., 2004; J. L. Elliott et al., 2010; J. Elliott & Freymueller, 2019; McAleer et al., 2009; Schartman et al., 2019). Several of these faults likely ruptured in the September 10, 1899 M_w~8.1 earthquake (Plafker & Thatcher, 2008). The ~9° difference in azimuth between Pacific and Yakutat motion also implies a component of Pacific-Yakutat convergence. This may be accommodated along the offshore Transition Fault (J. Elliott & Freymueller, 2019; Pavlis et al., 2004), as suggested by a M_w~6.4 and two $M_w \geq 5.4$ north-dipping thrust events at its southeast end in 1973 (Doser & Lomas, 2000; Figure 1a), although the extent and nature of present-day slip on the Transition Fault is debated (Christeson et al., 2010; Gulick et al., 2007).

2. Modeling of GIA, Stress Changes on Faults, and Earthquakes

We model the history of GIA-related deformation in southeast Alaska using the (preferred) GIA model of HF19, which couples a load history (Figures 2a–2d) with a layered elastic-viscoelastic Earth model. The load history consists of components representing the regionwide ice history and the post-1770 ice loss in Glacier Bay. The regionwide ice history was constructed by, in space, interpolating from the Berthier et al. (2010) distribution of late-20th-century ice thickness change and, in time, back-projecting the interpolated rates by a temporal function constructed by Larsen et al. (2005) based on previous abandoned moraines and glacial

Printed by [Nasa Goddard Space Flight - 156.068.119.100 - /doi/epdf/10.1029/2020JB020411] at [16/08/2021].

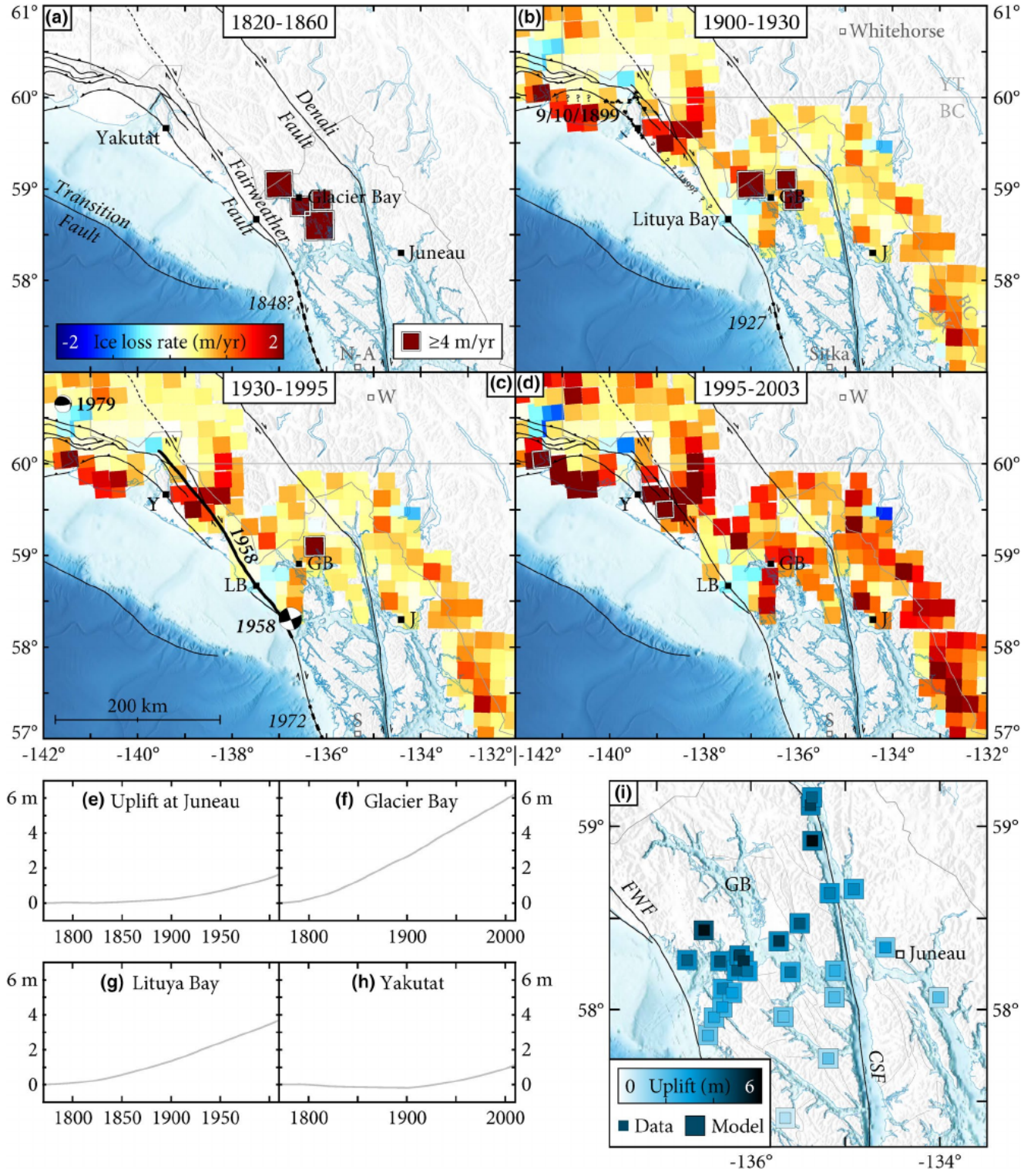


Figure 2. (a–d) Rates of ice loss in selected periods in the HF19 GIA model. Note that 19th-century ice loss in Glacier Bay is up to 10 m/yr. Rupture extent of 1848 earthquake (panel a) is unknown (supporting information Text S1). Black square points are selected locations for panels (e–h). (e–h) Model-predicted uplift histories at black square points in panels (a–d). (i) Comparison of Larsen et al. (2005) measurements of total 1770–2004 shoreline uplift (small colored squares) with model-predicted total 1770–2004 uplift at the same sites (large colored squares).

Printed by [Nasa Goddard Space Flight - 156.068.119.100 - /doi/epdf/10.1029/2020JB020411] at [16/08/2021].

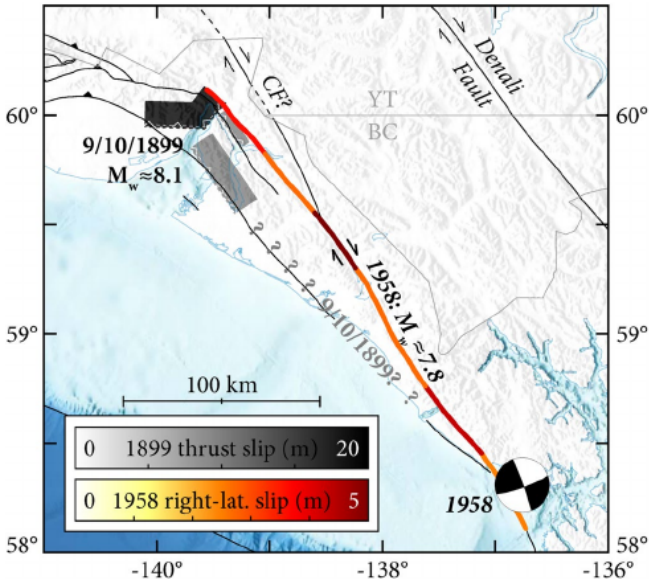


Figure 3. Slip models for the September 10, 1899 M_w~8.1 and 1958 M_w~7.8 earthquakes, respectively from Plafker and Thatcher (2008) and Doser (2010) (Section 4). Gray question marks denote hypothetical southeastward extension of September 10, 1899 rupture (Plafker & Thatcher, 2008), which we explore in models by laterally extending the southeasternmost slip source with 10 m of slip.

tramlines, and slightly modified by HF19. The Glacier Bay ice history is represented by additional load sources that follow individual time histories derived by Larsen et al. (2005).

The Earth model consists of a 55-km-thick elastic layer overlying a 230-km-thick Maxwell viscoelastic asthenosphere with viscosity 3×10^{19} Pa · s (and two deeper layers with much higher viscosities). In a three-dimensional search over lithosphere thickness, asthenosphere thickness and asthenosphere viscosity, HF19 found that this combination of the three parameters (coupled with the load history) produced the best fit to interannual uplift rates extracted from GPS data in southeast Alaska over 1992–2012. Although southeast Alaska features a complex juxtaposition of North American, Yakutat and Pacific lithosphere, the region of fastest uplift mostly consists of the Alexander Terrane of North America and the eastern Yakutat block (e.g., Colpron et al., 2007), which have similar seismic velocity structures (Morozov et al., 2001; Worthington et al., 2012), and so we think that a 1D Earth model is likely adequate. The uncertainties in Earth structure nonetheless contribute to the uncertainties in our subsequent modeling results, which are difficult to quantify.

HF19 used TABOO (Spada, 2003), which does not compute stress or allow for the addition of earthquake slip sources, so we convert the HF19 model to Relax (Barbot & Fialko, 2010; 2010b), using a uniform shear modulus of 52.5 GPa and a Poisson's ratio of 0.25 (supporting in formation Text S2). We henceforth refer to this as the HF19-R model. Despite the rheological simplifications in HF19-R, it reproduces present-day uplift rates well across our entire study area (Figure 1), and confirms that the rapid present-day uplift around Glacier Bay is mostly driven by the viscoelastic component of GIA (Figure S3), as inferred by Larsen et al. (2005). The HF19-R, HF19 and preceding models (J. L. Elliott et al., 2010; Larsen et al., 2004; 2005; Sato et al., 2011) do not incorporate the effects of mass redistribution from sea-level change, but in southeast Alaska that change is likely a sea-level fall at 5–9 mm/yr (Hill et al., 2011), 1–2 orders of magnitude smaller than the ice thickness change (Figures 2a–2d), and therefore likely has a second-order effect on GIA. The HF19-R model provides a good fit to Larsen et al. (2005) measurements of total 1770–2004 shoreline uplift (Figure 2i).

To compute stress changes and model earthquake slip on faults, we construct fault surfaces for the Fairweather-Queen Charlotte, Chatham Strait-Denali, Connector, and Transition faults and St. Elias thrust faults based on constraints from literature (Text S3). In most subsequent results, we use Relax to calculate the shear, normal, and Coulomb stress change on these fault surfaces at every model timestep, assuming an effective friction of 0.4 for Coulomb stress change (e.g., Harris & Simpson et al., 1998; King et al., 1994; Rice, 1992). An accompanying mapview-based approach for calculating stress changes is used and described in Section 4.5. In many of the models, we include stress changes from coseismic and postseismic deformation of the September 10, 1899 M_w~8.1 Yakutat Bay and 1958 M_w~7.8 Fairweather Fault earthquakes. For the September 10, 1899 event, we use the multi-segment slip model of Plafker and Thatcher (2008) (Figure 3), with optional along-strike extensions to the southeast and west, as described subsequently. For the 1958 earthquake, we use the slip model of Doser (2010) interpolated onto our modeled FWF surface (Figure 3), with slip prescribed as uniform from 0-15 km depth and zero below that. To incorporate these earthquakes into the stress change history, we add these coseismic slip models to the HF19-R model at timesteps corresponding to 1899 and 1958 and model their postseismic deformation as viscoelastic relaxation in the same asthenosphere that is undergoing GIA, so the two dynamically interact with each other. Modern-day GPS uplift rates are unaffected by these postseismic signals (Figure S4), and so the HF19 Earth model (which was derived from GPS uplift rates) remains robust even when accounting for them. Details of other earthquake locations, focal mechanisms and rupture extents are provided in Text S4.

Printed by [Nasa Goddard Space Flight - 156.068.119.100 - /doi/epdf/10.1029/2020JB020411] at [16/08/2021].

3. The Influence of GIA on Strike-Slip Faults

3.1. Previous Research

It is well established that GIA can influence seismicity in dip-slip settings (e.g., Adams, 1989; Hampel & Hetzel, 2006; Hetzel & Hampel, 2005; Steffen et al., 2014), but evidence is more scant in strike-slip settings. Johnston et al. (1998) showed that GIA following the Last Glacial Maximum (LGM) in Fennoscandia, the British Isles and Iceland would have in theory promoted strike-slip earthquakes outside the areas of the former ice loads. Muir-Wood (2000) showed how stress changes from removal of a disc load could combine with a strike-slip tectonic stress regime to yield alternating quadrants of enhanced and inhibited seismicity, with potential application to Fennoscandia and the British Isles. Physical evidence of such GIA-promoted strike-slip ruptures, however, is debated (Firth & Stewart, 2000), and potential links elsewhere are similarly ambiguous. James and Bent (1994) and Wu and Hasegawa (1996) inferred that post-LGM GIA does not explain modern-day strike-slip seismicity in eastern North America. Grollimund and Zoback (2001) proposed that post-LGM GIA could have triggered Holocene earthquakes in the New Madrid Seismic Zone if the stress changes were locally enhanced by a hypothesized low-viscosity zone at depth; however, those earthquakes have more recently been linked to stress changes from late Pleistocene erosion (Calais et al., 2010). The largest strike-slip earthquake that has been speculated as linked to GIA, to our knowledge, is the 1998 M_w~8.1 intraplate Antarctic plate event (Tsuboi et al., 2000), but that event's distance offshore made the influence of GIA difficult to prove or disprove (Kreemer & Holt, 2000). In contrast to Southeast Alaska, these other examples are from low-strain-rate regions.

Surface mass changes have also been linked to strike-slip earthquakes in non-GIA contexts. Luttrell et al. (2007) and Brothers et al. (2011) postulated that fluctuations of prehistoric Lake Cahuilla could have modulated the earthquake cycle on the southern San Andreas Fault. Luttrell and Sandwell (2010) and Neves et al. (2015) assessed how post-LGM sea-level rise could have modulated the stress on the San Andreas Fault and strike-slip faults in Portugal, respectively, although those effects would have occurred over timescales much longer than the rapid post-1770 deglaciation in southeast Alaska. Seasonal hydrological loading has also been shown to influence seismicity in strike-slip regimes in central California (Amos et al., 2014; Johnson et al., 2017; Kraner et al., 2018), New Madrid (Craig et al., 2017), central and southwest Japan (Heki, 2003), and possibly in south-central Alaska (Johnson et al., 2020). However, the load changes in these cases are on the order of <1 m equivalent water height, in contrast to the >1 km cumulative ice loss in Glacier Bay.

3.2. Reference Models for Physical Intuition (Figure 4)

To provide intuition into how ice loss and GIA could modulate the stress on strike-slip faults like the Fairweather Fault, we construct generic models of a 100 × 100 km square ice mass losing 1 m/yr equivalent water height atop or alongside a vertical right-lateral strike-slip fault, within the same Earth structure as the HF19-R model for southeast Alaska. We compute the shear, normal and Coulomb stress changes on the fault through 200 years of constant ice loss and elastic-viscoelastic GIA. Shear stress changes are computed for right-lateral slip and we assume an effective friction of 0.4.

These models yield several results that inform our subsequent analysis in southeast Alaska. If the decreasing load is centered over the fault (Figure 4a), GIA unclamps the fault (decreases the normal or confining stress on it) because the lithospheric rebound beneath the load includes an outward radial component of motion (e.g., Figure 1a, horizontal vectors), and so the Coulomb stress on the fault is increased by up to 0.6 MPa (6 bars) beneath the load center. If the fault runs along the edge of the decreasing load (Figure 4b), the unclamping is milder but is accompanied by a shear stress change that is antisymmetric about the load, yielding an asymmetric pattern of Coulomb stress change with a maximum Coulomb stress increase for right-lateral slip of 0.5 MPa (5 bars) at the corner of the load. If the fault runs 50 km from the edge of the decreasing load (Figure 4c), the shear stress changes are milder and the fault is clamped shut because it is in the forebulge, where horizontal motions are radially inward rather than outward; therefore Coulomb stress is decreased over more of the fault than it is increased. Finally, if the fault runs along the opposite edge of the decreasing load (Figure 4d), the unclamping is the same as in Figure 4b but the shear and therefore the

Printed by [Nasa Goddard Space Flight - 156.068.119.100 - /doi/epdf/10.1029/2020JB020411] at [16/08/2021].

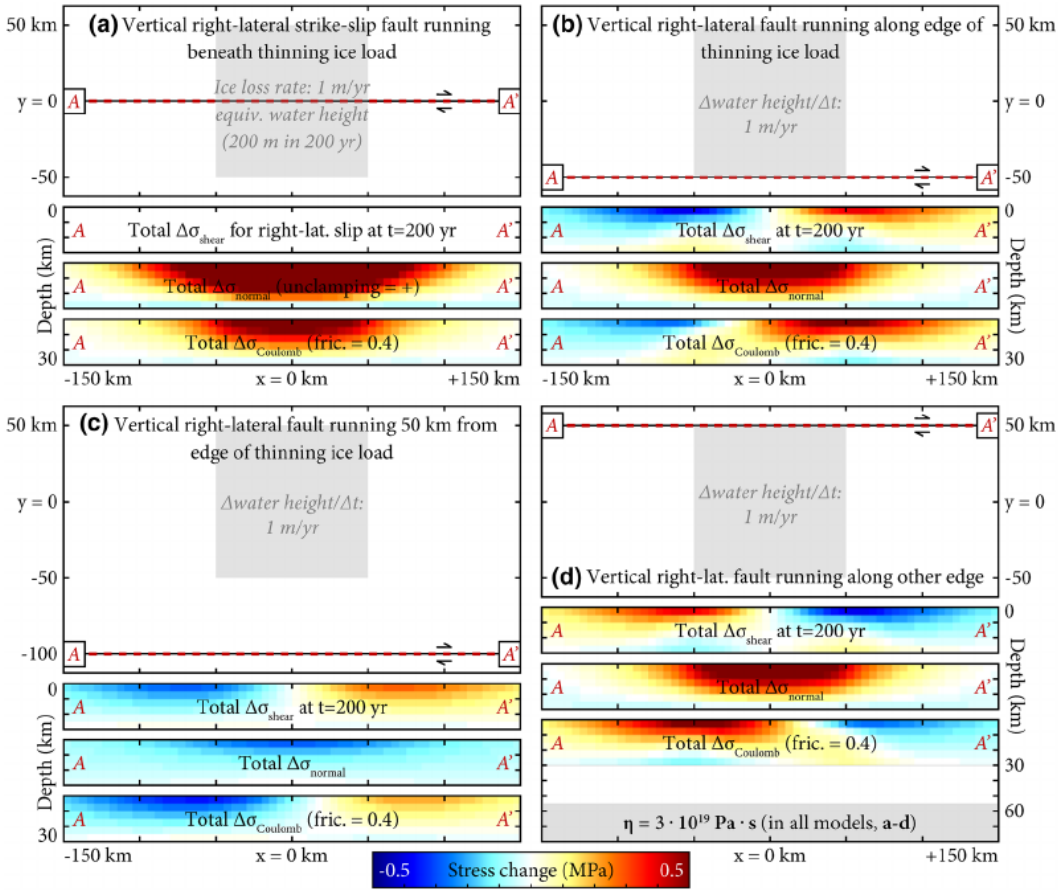


Figure 4. Cumulative 200-year stress changes imparted to a vertical right-lateral strike-slip fault by GIA associated with an ice load steadily losing 1 m/yr equivalent water height (gray) (Section 3.2). Four different configurations are shown: a) the fault runs beneath the center of the thinning ice load; b) the fault runs along the edge of the ice load; c) the fault runs 50 km (the load half-width) from the edge of the ice load; d) the fault runs along the opposite edge of the ice load. Earth model is the HF19-R model used in southeast Alaska (Section 2). Cross section profiles A-A′ are along the fault.

Coulomb stress change distributions are reversed. These results are generalizable to other cases of GIA in strike-slip settings, as a complement to the models of Muir-Wood (2000).

4. Results

4.1. GIA-Induced Stress Changes and the 1958 Fairweather Fault Earthquake (Figures 5 and 6)

We then use the HF19-R model to compute the history of stress changes imparted by post-1770 ice loss and GIA to faults in southeast Alaska. This yields our main finding: that the location of maximum GIA-induced Coulomb stress increase on the Fairweather Fault as of 1958 was very close to the epicenter of the 1958 M_w~7.8 Fairweather Fault earthquake (Figures 5a and S6a). The 1958 epicenter was located on the only section of the FWF on which GIA had induced both unclamping (Figure 5c) and a shear stress increase for right-lateral slip (Figure 5b). Comparing with the reference models of GIA and stress change in Section 3.2, the FWF lies within 100 km of the past ice loss in Glacier Bay (Figures 1a, 2a and 2b), close enough that GIA from that ice loss unclamped (Figures 4b and 5c) rather than clamped it (Figure 4c). Shear stress for right-lateral slip was increased around the 1958 epicenter (Figure 5b) because the south-southeast component of GIA-related deformation was larger on the east side of the fault than on the west side (e.g., Figure 1a, horizontal vectors), inducing a net right-lateral shear stress. Summing these two effects, the 1958 epicenter was analogous to the location of maximum Coulomb stress change near the corner of the

Printed by [Nasa Goddard Space Flight - 156.068.119.100 - /doi/epdf/10.1029/2020JB020411] at [16/08/2021].

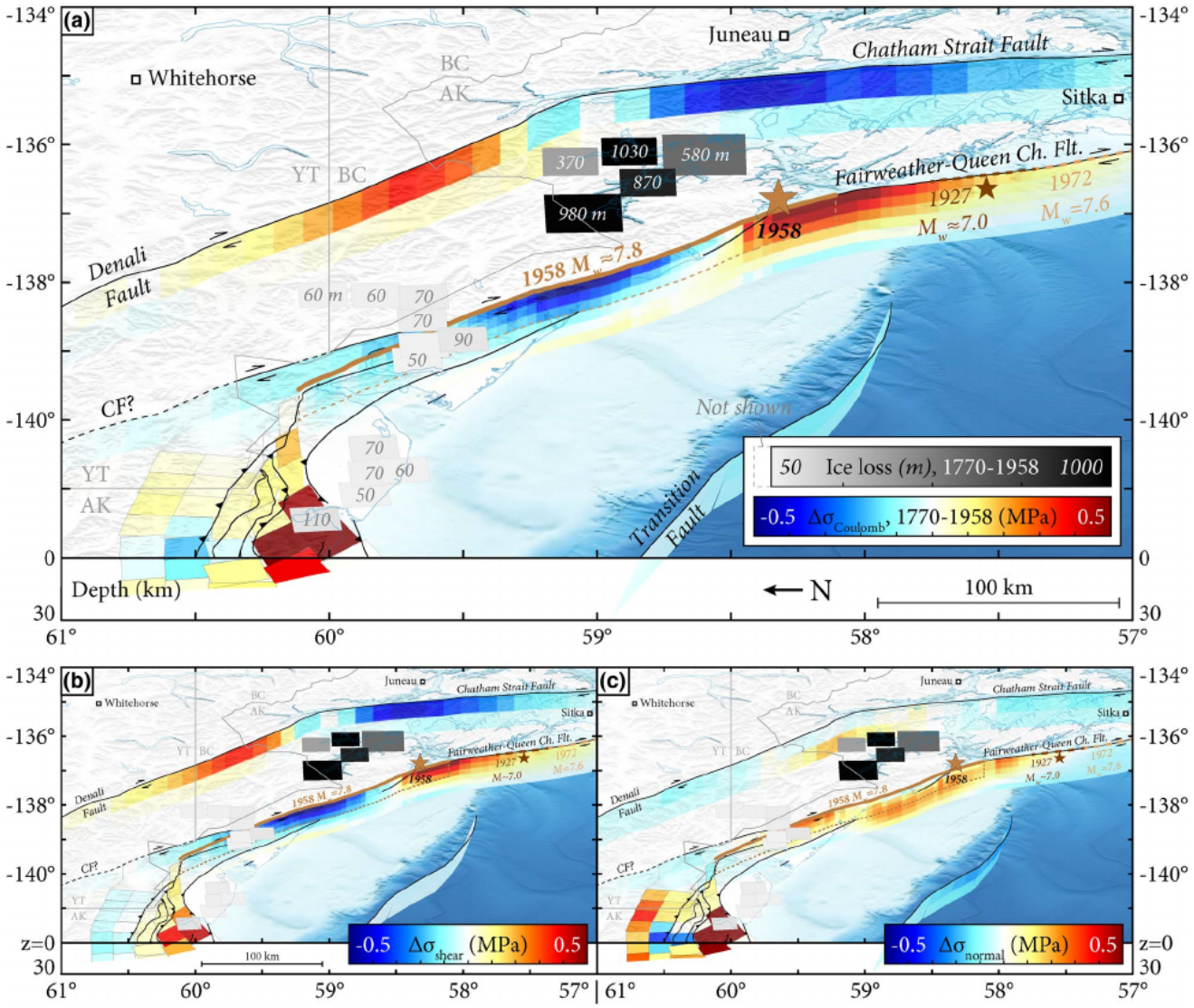


Figure 5. Cumulative ice loss (grayscale squares and italics) and GIA-related stress changes (colored patches) on major faults between 1770 and 1958. Fault surfaces and rakes are described in Section 4. Brown stars: epicenter of 1958 M_w~7.8 Fairweather Fault earthquake (Doser & Lomas, 2000). Dashed brown lines: 15-km depth line on 1958 rupture. (a) Cumulative Coulomb stress changes assuming an effective friction of 0.4. (b) Shear stress changes. (c) Normal stress changes, positive for unclamping.

decreasing load in the example in Figure 4b. These combined effects also mean that the 1958 epicenter was located near the maximum GIA-induced Coulomb stress increase on the FWF regardless of the effective friction assumed (Figure S8a).

Assuming an effective friction of 0.4 and that a shear modulus of 52.5 GPa (Section 2) applies along faults, the total 1770–1958 GIA-induced Coulomb stress increase at the 1958 epicenter was ~0.6 MPa (6 bars) at 2.5 km depth, ~0.3 MPa (3 bars) at 12.5 km depth and ~0.2 MPa (2 bars) at 17.5 km depth. (The Doser and Lomas [2000] hypocentral depth for the 1958 event is 16 km.) These results are not strongly dependent on the elastic-viscoelastic structure in the GIA model (Figures 6 and S7), although uncertainties in Earth structure mean that the order of magnitude of stress changes is more robust than the specific numerical values.

The time evolution of stress change on faults shows that most of the pre-1958 Coulomb stress increase at the 1958 epicenter had occurred by 1900 (Figure S9c). More instructive is an auxiliary model in which ice

Printed by [Nasa Goddard Space Flight - 156.068.119.100 - /doi/epdf/10.1029/2020JB020411] at [16/08/2021].

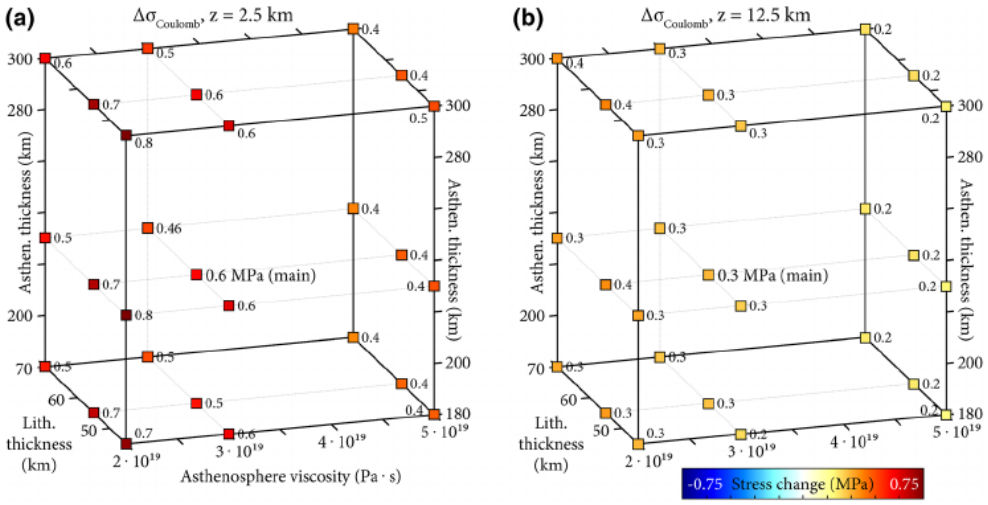


Figure 6. Effect of the Earth model on GIA-induced Coulomb stress changes at the epicenter of the 1958 Fairweather Fault earthquake. Hu and Freymueller (2019, their Table 1) give preferred and one-sigma values for the Maxwell viscosity of the asthenosphere and the thicknesses of the lithosphere and asthenosphere. This yields 27 possible combinations of the three parameters, which we model here by substituting those parametrizations into the HF19-R model (Section 4). Colored squares and numbers give the cumulative 1770–1958 GIA-induced Coulomb stress changes (effective friction 0.4) at the 1958 epicenter in each of the 27 models, at 2.5 (a) and 12.5 (b) km depth. Results from HF19's preferred combination of the three parameters are indicated with larger text. Note that Doser and Lomas (2000) infer a hypocentral depth of 16 km for the 1958 earthquake.

loss is stopped in 1900 (and thus confined entirely to Glacier Bay) but viscoelastic relaxation from this ice loss continues after 1900. This model (Figure S9e) yields a similar Coulomb stress change pattern on the FWF as of 1958 to that of the main model (Figure 5a), showing that most of the GIA-induced stress change on the FWF—including the stress increase at the 1958 epicenter—resulted from the rapid 19th-century ice loss in Glacier Bay and the viscoelastic response to that ice loss. Furthermore, the pre-1958 stress changes on the FWF mostly resulted from viscoelastic deformation rather than the elastic response to short-term interannual ice loss (Figures S10e–S10f). Together, these results indicate that the pre-1958 stress changes specifically mostly resulted from the viscoelastic response to 19th-century ice loss in Glacier Bay.

4.2. Comparison of GIA-Induced and Tectonic Stress Changes Along the Fairweather Fault

The estimated GIA-induced ~0.2–0.6-MPa Coulomb stress increase at the 1958 epicenter is likely equivalent to the stress change from only ~5 years of shear loading on the fast-slipping QC-FWF (Figures S7c and S7d). As such, GIA likely was a second-order contributor to stress on the FWF, with tectonic loading being the main driver. The 1958 surface rupture also included up to 1 m of southwest-side-up dip slip at the surface (Tocher, 1960); this would have been inhibited by pre-1958 GIA (Figure S8b), as the lithospheric rebound northeast of the FWF in Glacier Bay would have instead promoted northeast-side-up motion on the fault. The SW-side-up dip slip may be more plausibly explainable as a product of NE-directed tectonic compression (J. Elliott & Freymueller, 2019; McAleer et al., 2009; Schartman et al., 2019). This too suggests that tectonic loading is likely the main driver of earthquake behavior on the FWF, although the timing of failure may be influenced by GIA.

4.3. The 1958 Rupture and Stress Changes From the September 10, 1899 M_w~8.1 Earthquake (Figures 7 and 8)

The 1958 earthquake ruptured unilaterally northwestward from the epicenter (Doser, 2010). In addition to increasing the shear and Coulomb stress on the FWF near the 1958 epicenter, pre-1958 GIA likely unclamped most or all of the 1958 rupture (Figure 5c). However, it would also have decreased the shear and thus the Coulomb stress along the rupture northwest of the epicenter (Figures 5a and 5b), even given a larger effective friction coefficient (Figure S8a), and therefore would have in principle somewhat disfa-

Printed by [Nasa Goddard Space Flight - 156.068.119.100 - /doi/epdf/10.1029/2020JB020411] at [16/08/2021].

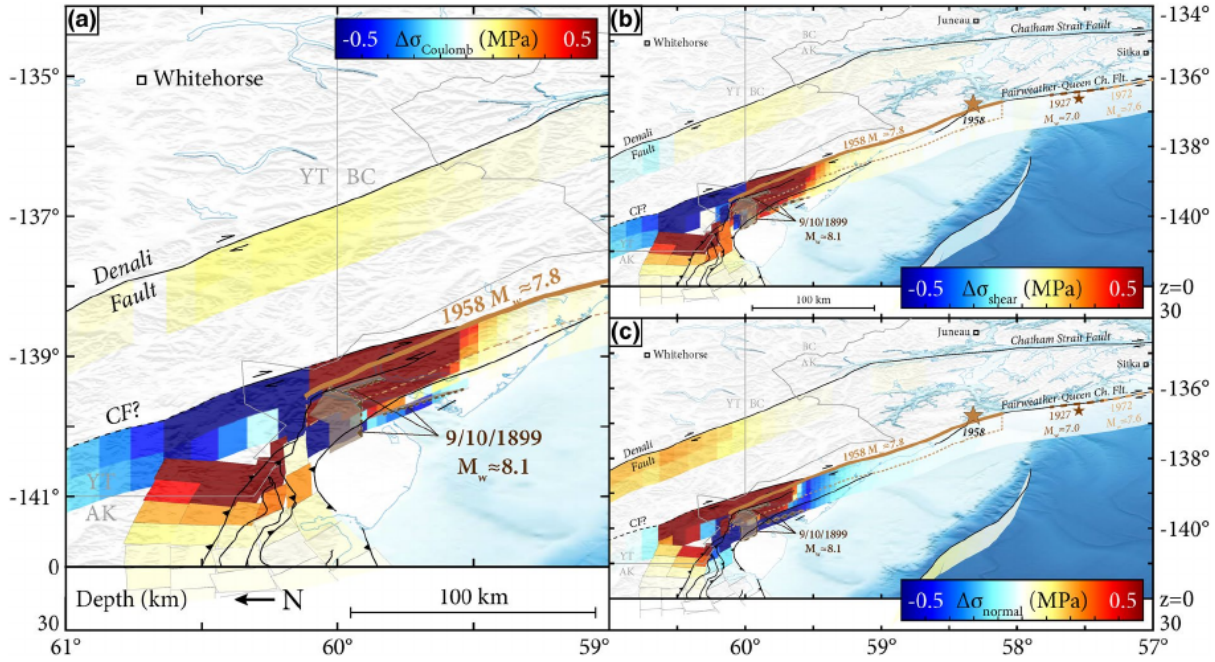


Figure 7. Stress changes imparted by the September 10, 1899 M_w~8.1 Yakutat Bay earthquake to nearby faults (colored patches). Brown shape is Plafker and Thatcher (2008) slip model for 1899 earthquake; slip is assumed pure reverse on all segments. (a) Coulomb stress changes assuming an effective friction of 0.4. (b) Shear stress changes. (c) Normal stress changes, positive for unclamping.

vored the northwestward propagation of the rupture. (This effect is also seen on the left side of the fault in the reference models in Figures 4b and 4c.) In the Section 5, we discuss two factors that could have potentially counteracted this shear stress decrease (dynamic rupture propagation and time since the last rupture). A third factor that may have promoted northwestward propagation in the 1958 earthquake was the stress change imparted by the 1899 M_w~8.1 Yakutat Bay earthquakes, particularly the September 10, 1899 M_w~8.1 event, which likely ruptured multiple thrust or oblique-thrust faults seaward of the FWF (Figure 3). Using the Plafker and Thatcher (2008) dislocation model for the September 10, 1899 earthquake, we calculate that that event increased both the shear and normal stress on the northwest end of the future 1958 rupture (Figure 7). The September 10, 1899 event also may have also ruptured further southeast down the coast (Plafker & Thatcher, 2008), and if so it would have unclamped more of the 1958 rupture (Figure S11), although the total Coulomb stress effect on the FWF depends on whether slip on the southeast extension was closer to pure reverse (Figure S9) or right-reverse (Figure S12). Still, despite uncertainties in the rupture geometry and slip distribution, we conclude that the September 10, 1899 event likely promoted failure on at least the northwest section of the 1958 rupture (Figures 7, S11 and S12). (The September 4, 1899 M_w~8.1 event was further west and likely had a lesser stress effect, Figure S13). The combination of GIA and the September 10, 1899 event would therefore have promoted failure along much of the 1958 rupture (Figure 8).

The time evolution of Coulomb stress at three points on the FWF in this combined model shows that although the near-field stress change in the September 10, 1899 event may have been very large (Figure 8b, yellow line), stress was rising faster at the 1958 epicenter (red line) than along any other part of the FWF before 1958 (even accounting for postseismic deformation of the September 10, 1899 event (Figure S13), which is included in the model in Figure 8 as described in Section 4); therefore the epicenter was approaching the Coulomb failure threshold faster than anywhere else on the FWF. This is relevant because: (1) the absolute stress at any point on the fault is unknown, so each of the lines in Figure 8b could be shifted up or down; and (2) the magnitude and distribution of slip in the September 10, 1899 event is highly uncertain. Therefore it is not known how close any point on the FWF was to failure in an absolute sense.

Printed by [Nasa Goddard Space Flight - 156.068.119.100 - /doi/epdf/10.1029/2020JB020411] at [16/08/2021].

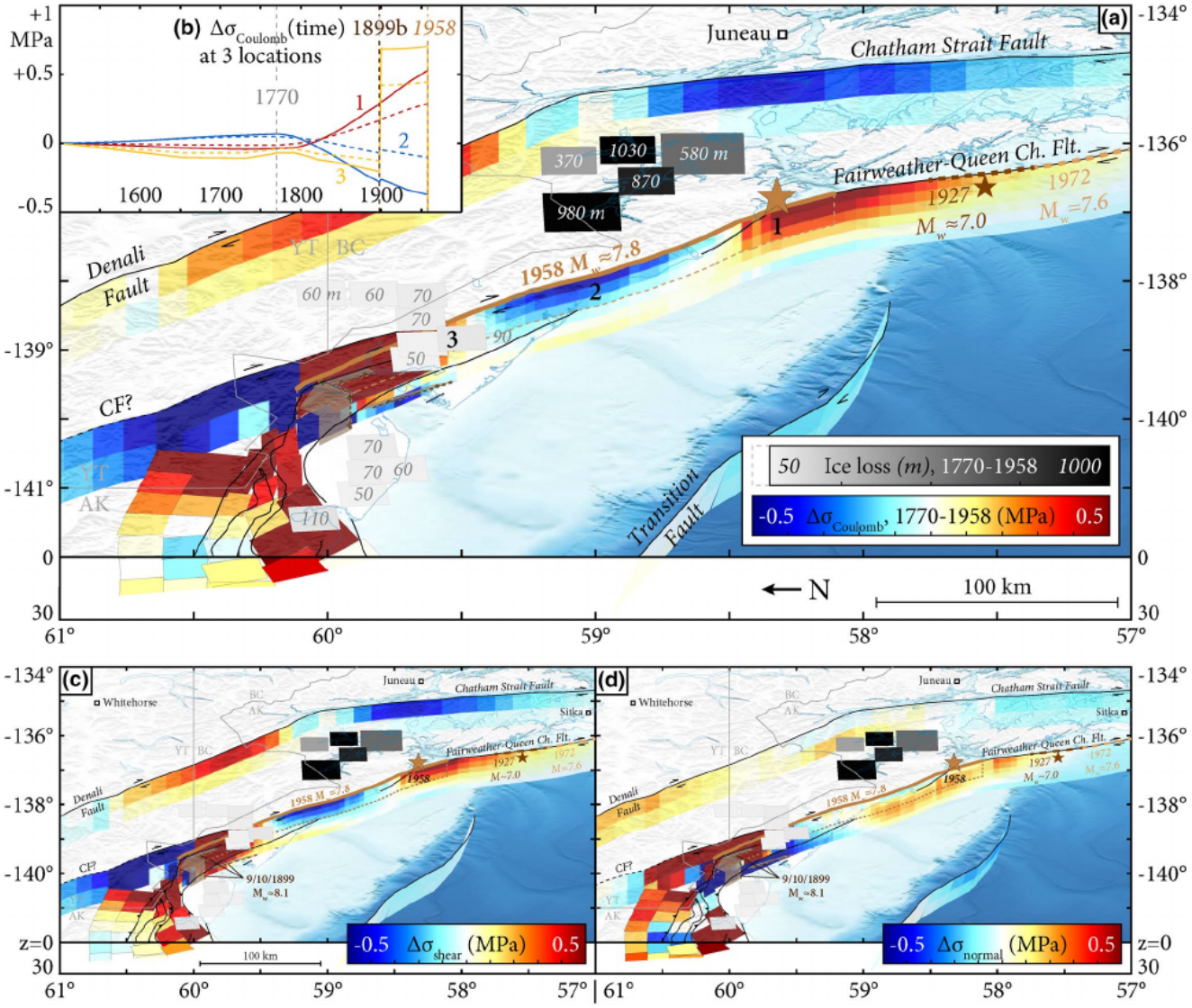


Figure 8. Cumulative ice loss (grayscale squares and italics) and stress changes on faults (colored patches) induced by GIA and by coseismic and postseismic (viscoelastic) deformation of the September 10, 1899 M_w~8.1 Yakutat Bay earthquake, between 1770 and 1958. (a) Cumulative Coulomb stress changes assuming an effective friction of 0.4. (b) Evolution of Coulomb stress changes at three points on the Fairweather Fault labeled in panel a, at 2.5 km depth (solid lines) and 12.5 km depth (dashed). Note that starting stress values are arbitrary. (c) Cumulative shear stress changes from GIA and September 10, 1899 earthquake. (d) Cumulative normal stress changes, positive for unclamping.

4.4. GIA- and Earthquake-Induced Stress Changes on Thrust Faults in the St. Elias (Figure 9)

We find that GIA also increased the Coulomb stress on north-dipping thrust faults of the St. Elias margin (Figures 5a and 9a), in agreement with Sauber and Molnia (2004) and Sauber and Ruppert (2008). In contrast to the FWF, this GIA-related stress change predominantly resulted from post-1900 ice loss overlying these faults (Figures 2b, 2c, S7d, and S7f), which would have unclamped them (Figure 5c) and increased the shear stress for oblique-reverse slip on them (Figure 5b; J. Sauber et al., 2000). At the epicenter of the 1979 M_w~7.4 St. Elias earthquake, beneath the Bagley Ice Valley and Jeffries Glacier, the HF19-R model indicates that pre-1979 GIA should have inhibited failure (Figure 9a). However, this result is likely not robust: the HF19 ice history model parametrizes these as accumulation zones throughout the 20th century (Figure 2c) based on extrapolation from Berthier et al. (2010) late-20th-century ice thickness change rates, but in reality they are likely not accumulation zones over the long term (Muskett et al., 2003). Our GIA model does

Printed by [Nasa Goddard Space Flight - 156.068.119.100 - /doi/epdf/10.1029/2020JB020411] at [16/08/2021].

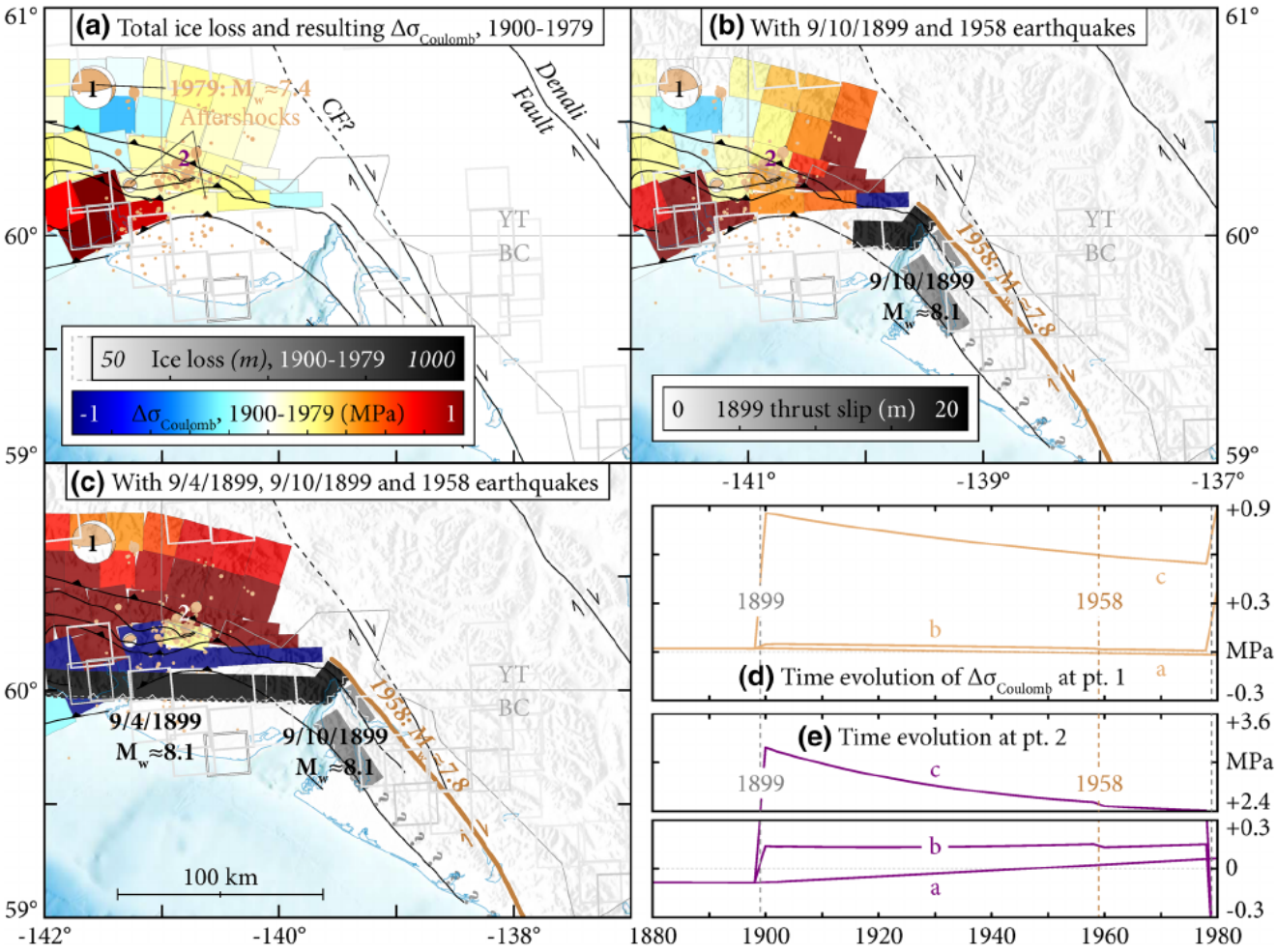


Figure 9. Cumulative Coulomb stress changes imparted to thrust faults in the St. Elias (colored patches) by post-1770 GIA and by coseismic and postseismic (viscoelastic) deformation of the 1899 and 1958 earthquakes, as of 1979 (Figure 8 shows 3D geometry of thrust surface). (a) Coulomb stress changes solely from 1770 to 1979 GIA. (b) Coulomb stress changes from 1770 to 1979 GIA and coseismic and postseismic deformation from the September 10, 1899 and 1958 earthquakes. (c) Same as (b) but adding speculative slip model of the September 4, 1899 M_w~8.1 thrust earthquake, modeled as 20 m of pure reverse slip extending west from the west end of the September 10, 1899 source to Cape Yakataga. (d and e) Time evolution of Coulomb stress change at locations 1 and 2 in the models in panels a–c. Location 1 is epicenter of 1979 M_w~7.4 St. Elias earthquake; location 2 is cluster of aftershocks of 1979 earthquake.

promote failure at the location of the 1979 earthquake's dense aftershock sequence (Figure 9a), consistent with Sauber and Ruppert (2008).

The September 10, 1899 M_w~8.1 Yakutat Bay and 1958 M_w~7.8 FWF earthquakes also promoted failure on thrust faults in the St. Elias, possibly including an area of dense aftershock activity following the 1979 earthquake (Figure 9b). More speculatively, the September 4, 1899 M_w~8.1 event may have also promoted failure on St. Elias thrust faults (Figure 9c). This depends on its location and extent; the Doser (2006) relocated epicenter is 59.43°N, 143.05°W, and the observation of an uplifted terrace at Cape Yakataga (Plafker & Thatcher, 2008) suggests that the September 4, 1899 event may have been a shallow thrust earthquake like the September 10, 1899 event six days later, but this remains speculative.

4.5. GIA's Overall Effect on Earthquakes in Southeast Alaska (Figure 10)

To assess the overall effect of post-1770 GIA on recorded earthquakes in southeast Alaska, we compile a unified earthquake catalog for the region from 1920 to present (supporting information Text S4) and use the HF19-R model to calculate the GIA-induced stress changes at the sites and times of these earthquakes. Within an area extending from 57° to 61° N and from 142° to 132° N, the unified catalog includes

Printed by [Nasa Goddard Space Flight - 156.068.119.100 - /doi/epdf/10.1029/2020JB020411] at [16/08/2021].

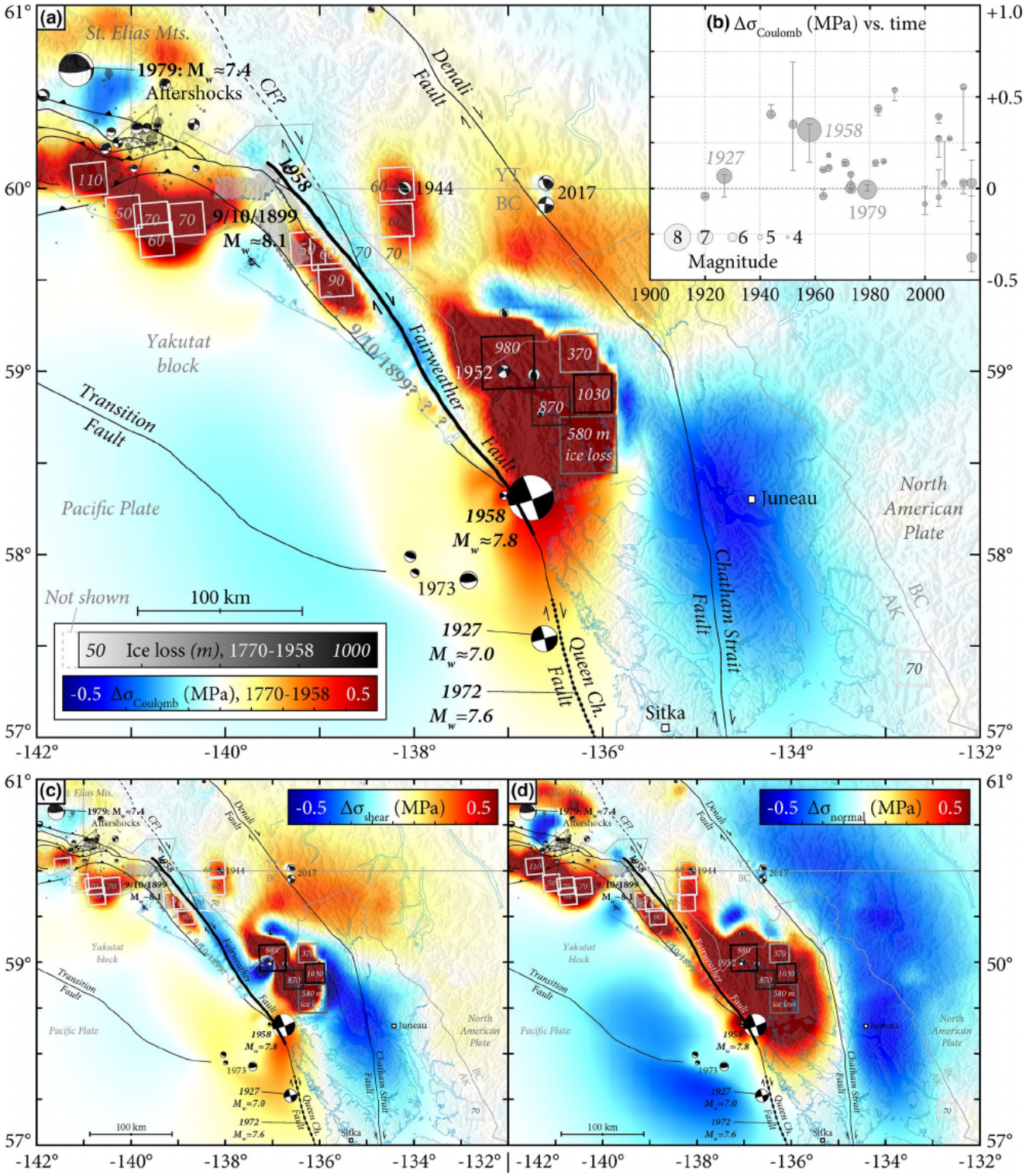


Figure 10. $M_w \geq 5.0$ earthquakes and stress changes imparted by post-1770 GIA to their fault planes and slip senses (focal mechanisms plotted). Earthquakes are described in supporting information Text S4 and Section 4. Stress changes (colored surfaces) are calculated at 10 km depth on a grid of receiver fault orientations and slip senses interpolated from those of major faults (including St. Elias and September 10, 1899 thrust planes) and nodal planes of $M_w \geq 5.0$ events (Section 9). (a) Coulomb stress changes as of 1958. (b) Cumulative GIA-induced Coulomb stress changes at the epicenters of earthquakes as of their occurrence times. Errorbars show 16th- and 84th-percentile values for stress changes at epicenters that earthquake strikes have (one-sigma) uncertainties of 30°. (Note that for example, the 1958 earthquake has a strike uncertainty of far less than 30° as it is known to have occurred on the Fairweather Fault; this is also very likely the case for the 1927 event, among others.) (c) Shear stress changes as of 1958. (d) Normal stress changes as of 1958, positive for unclamping.

Printed by [Nasa Goddard Space Flight - 156.068.119.100 - /doi/epdf/10.1029/2020JB020411] at [16/08/2021].

30 $M_w \geq 5.0$ earthquakes. Assuming an effective friction of 0.4, we calculate that post-1770 GIA promoted failure in 23 of these 30 events as of their occurrence times (Figure 10b). Seven events occurred at locations of decreased Coulomb stress (including the 1979 St. Elias event, which may not be a robust result as discussed above). 22 of the 30 $M_w \geq 5.0$ events occurred at locations of increased shear stress as resolved onto their cataloged slip planes, 19 occurred at locations where their fault planes were likely unclamped, and 15 occurred at locations where both occurred (as with the 1958 event). (23 of 30 events would still have been promoted if the effective friction coefficient were 0.8.)

To show this graphically and to complement Figures 5–9, we make mapview plots of GIA-related stress changes on a grid of representative fault orientations throughout Southeast Alaska. We derive 2D grids of local fault orientations (Figure S15) and slip senses (Figure S16) by spatially interpolating from our fault model (Section 2; we add the Plafker and Thatcher [2008] model of the September 10, 1899 earthquake) and from the strikes, dips and rakes of $M_w \geq 5.0$ events in the unified catalog, using natural-neighbor interpolation in MATLAB. We then calculate the history of the stress change tensor at 10 km depth and resolve the stress changes on the gridded fault planes and rakes. Figures 10a–10d show the distributions of Coulomb, shear and normal stress changes as of 1958. (Figure S6 shows an example for a uniform receiver fault orientation based on the strike, dip and rake of the 1958 FWF earthquake; Figure S17 shows the result if the fault orientation grid is interpolated only from major fault surfaces, with focal mechanisms excluded.) When incorporating the coseismic and postseismic deformation of the September 10, 1899 and 1958 earthquakes (Figure S18), 24 of 30 $M_w \geq 5.0$ events would have been promoted and six inhibited.

As one test of whether the number of GIA-promoted $M_w \geq 5.0$ events is meaningful, we use these maps to assess how many of the 30 recorded $M_w \geq 5.0$ events would have been promoted if they had occurred at random locations within our map area. We run 100 models in which we compute the Coulomb stress change at sets of 30 random points within the map area as interpolated from the distribution in Figure 10a. In these 100 models, the mean and median number of promoted locations are 11.26 and 11 out of 30, respectively, and none of the 100 models has more than 17 promoted locations out of 30, in contrast to the 23 in the real set. (If one interpolates the stress changes from the distribution in Figure S6a, in which the fault orientation grid is based only on major fault surfaces, the mean, median and maximum in 100 are 9/30, 9/30, and 15/30, respectively.)

5. Discussion

5.1. Factors Promoting Failure and Rupture Propagation in the 1958 Fairweather Fault Earthquake

Our key finding is that post-1770 GIA, in particular the viscoelastic response to 19th-century ice loss in Glacier Bay, likely promoted Coulomb failure at the epicenter of the 1958 M_w~7.8 Fairweather Fault earthquake. The 1958 epicenter coincides with the largest GIA-related Coulomb stress increase on the FWF (Figure 5; Section 4.1). Pre-1958 GIA also unclamped most or all of the 1958 rupture zone (Figure 5c); however, it also decreased the shear and Coulomb stress on the FWF northwest of the epicenter (Figures 5a and 5b), which in principle should have inhibited the northwestward rupture in the earthquake. However, the September 10, 1899 M_w~8.1 Yakutat Bay earthquake likely increased the Coulomb stress on at least the northwest end of the FWF, possibly counteracting the effect of GIA there (Figures 7 and 8; Section 7).

Two other factors may have additionally promoted northwestward rupture in the 1958 earthquake. The first is stress transfer during rupture propagation. During a strike-slip rupture, the slip that has occurred should quasi-statically promote shear failure beyond the rupture tip, which could overcome the GIA-induced shear stress decrease. As the 1958 earthquake was not a supershear event (Doser, 2010), shaking from the slip that had occurred at a given time would have also dynamically modulated the shear stress state beyond the propagating rupture tip. In addition, slip on a bimaterial interface (which the FWF likely is) should induce a dynamic reduction in the normal stress (Ben-Zion, 2001; ten Brink et al., 2018; Weertman, 1980), which would have compounded the GIA-induced unclamping (Figure 5c) and further promoted rupture.

The second factor is that the FWF northwest of the 1958 epicenter may have been particularly "due" for rupture. In the relocations of Doser and Lomas (2000) and the historical record of Sykes et al. (1981), the only

Printed by [Nasa Goddard Space Flight - 156.068.119.100 - /doi/epdf/10.1029/2020JB020411] at [16/08/2021].

two pre-1958 events attributed to the QC-FWF are the 1927 M_w~7.0 event to the southeast (Figure 5a) and the 1848 M_w~7.5 event near Sitka (then Novo-Arkhangelsk) (Figure 2a), which may have been similar to the 1972 M_w = 7.6 Sitka earthquake (supporting information Text S1). Therefore, it is possible that the 1958 rupture zone had not ruptured since at least 1848 (Sykes et al., 1981) and perhaps in even longer if the 1848 event was further south, whereas the QC-FWF to the southeast had likely ruptured in 1927 and perhaps in 1848. Plafker et al. (1978) and Koehler and Carver (2018) estimate the recurrence interval for earthquakes on the FWF to be 60–110 years and 70–155 years, respectively, consistent with the 110-year interval between 1848 and 1958). However, historical earthquake records in this region may be incomplete, particularly along the remote coast spanned by the 1958 rupture. Previous large waves (local tsunamis) likely occurred in Lituya Bay in ca. 1853–1854, ca. 1874 and ca. 1899 (Miller, 1961), any of which could have in theory been triggered by a nearby earthquake. (The ca. 1899 wave may have been triggered by the September 10, 1899 M_w~8.1 Yakutat Bay shock or by a nearby event it triggered [Miller, 1961].) An uncatalogued earthquake was also felt in Lituya Bay on 30 August 1933, and Jim Huscroft, the sole permanent resident of Lituya Bay between 1915 and 1917 and 1939, described earthquakes as "a frequent occurrence in the bay" (Fradkin, 2001). Nevertheless, the instrumental evidence for the M_w~7.0 shock to the southeast in 1927 (Doser & Lomas, 2000) and the lack of instrumental evidence of any other pre-1958 events on the FWF suggests that the northwestward rupture in 1958 may have been favored by a lack of large recent ruptures on that section of fault, with GIA-induced stress changes perhaps favoring the 1958 epicenter as the first point of failure.

A follow-on question is whether the 1927 M_w~7.0 event itself could have promoted failure in 1958. Using the Doser and Lomas (2000) rupture extent and modeling coseismic and postseismic deformation with the HF19-R earth model, we infer that the 1927 event likely occurred too far south to have an appreciable stress effect on the 1958 rupture (Figure S8e), although this depends on the extent of rupture in 1927. If there were indeed a gap between the 1927 and 1958 rupture zones (Figure S8e), it could also have been filled by a smaller, uncatalogued event (presumably early in the 20th century or before that), aseismic slip, or some combination thereof, any of which could have promoted failure in 1958. We calculate that the 1949 M_w~7.9 QCF earthquake likely had no stress effect at the 1958 epicenter (Figure S8e). Poroelastic relaxation of the elastic stress changes during GIA also likely had only a small effect on fault stress over the 1770–1958 period compared to the effect of GIA itself (Figure S19). GIA also may have promoted failure in the 1927 earthquake (Figure 5a) and possibly the 1848 event (Figure S8b; supporting information Text S1), depending on their rupture extents.

Finally, we note that the 1958 earthquake occurred in July, the warmest month of the year in Southeast Alaska (http://oldclimate.gi.alaska.edu/Climate/Location/TimeSeries/Juneau.html; http://oldclimate.gi.alaska.edu/Climate/Location/TimeSeries/Yakutat.html), when seasonal ice loss would have been at its most rapid. 1958 was also the warmest year in the region since 1944 (see same references), which would presumably have further enhanced short-term ice loss. While the magnitude and distribution of this ice loss is unknown, the major topographic feature of the 1958 epicentral region is the high Fairweather Range, which lies north of the epicenter and on the northeast side of the FWF, contrasting with lower, less glaciated topography and the shore on the southwest. If the largest summer snow and ice loss occurs within the Fairweather Range, it would also increase the Coulomb stress at the 1958 epicenter (Figures 4b and 4c). Therefore, the high temperature of 1958 and the month of July could have also promoted failure at the epicenter. (The same would not apply to the 1979 M_w~7.4 St. Elias earthquake, which occurred in late February, although it could perhaps apply to the September 1899 M_w~8.1 earthquakes [J. Sauber & Ruppert, 2008].)

5.2. Impact of GIA-Induced Stress Changes on Earthquake Probabilities on the Fairweather Fault

In the context of the rapid tectonic loading on the FWF, we can quantitatively assess the significance of the GIA-induced stress change at the 1958 epicenter by estimating its impact on earthquake probabilities. We assume that the GIA-induced stress change has the effect of reducing the FWF's earthquake recurrence interval (e.g., Working Group on California Earthquake Probabilities, 1990), as if the fault were being loaded faster (which may be viable to first order as the stress change occurred gradually). Assuming that the stress change accrued linearly between 1770 and 1958 and was in total equivalent to a 5-year reduction in recurrence interval over that time (Section 4.2), it translates to a 2.7% reduction in recurrence interval. We

Printed by [Nasa Goddard Space Flight - 156.068.119.100 - /doi/epdf/10.1029/2020JB020411] at [16/08/2021].

then assume that FWF earthquakes follow a stationary Poisson process in which the probability at least one event in timespan t given recurrence interval R is 1 – exp (-t/R). Assuming a background recurrence interval of 70 years (R. Koehler & Carver, 2018), the 50-year probability of at least one earthquake on the FWF without GIA would be 1 – exp (–50/70) = 51.1%, whereas with the GIA-induced stress change it would be 1 – exp (–50/(70–0.027 × 70)) = 52.0%, a probability gain of 0.9%. If the background recurrence interval were instead 155 years (R. Koehler & Carver, 2018), GIA would change the 50-year probability of at least one event from 27.6% to 28.2%. These subtle changes underline that the contribution of GIA is likely second-order in the context of the rapid tectonic loading in southeast Alaska. This parallels the finding that aftershock activity is controlled more by the preexisting stress state than by the stress changes in earthquakes (Segou & Parsons, 2020).

5.3. Promotion of Failure in Other $M_w \geq 5.0$ Events by GIA

We find that post-1770 GIA likely promoted Coulomb failure in at least 23 of the 30 $M_w \geq 5.0$ earthquakes recorded in southeast Alaska since 1920 (Figure 10), a correlation well above what randomized models would predict (Section 4.5). (Note that GIA's impact on the 1899 M_w~8.1 earthquakes is poorly constrained as regionwide ice loss is estimated to have begun ca. 1900). This suggests that although rapid tectonic loading is the first-order driver of stress and earthquake activity in this region, GIA may nevertheless play an accompanying role (perhaps promoting earthquake occurrence in time), as inferred by Sauber and Molnia (2004) and Sauber and Ruppert (2008) in the St. Elias. For comparison, the estimated ~0.2–0.6-MPa Coulomb stress increase at the 1958 Fairweather Fault earthquake's epicenter is well above the estimated ~0.01–0.02-MPa threshold value needed for static stress changes to impact seismicity (Hardebeck et al., 1998; Rydelek & Sacks, 1999). Although GIA has been frequently linked to dip-slip earthquakes (Section 3), the southeast Alaska example shows that it may also affect strike-slip earthquakes. This may be applicable (Figure 4) to other cases of rapid GIA in proximity to strike-slip faults, as for example in northern Patagonia (Dietrich et al., 2010; Wang et al., 2007) and possibly along the Alpine Fault in New Zealand (e.g., Chinn et al., 2012).

5.4. Stress Interactions Between the Fairweather Fault, St. Elias Margin and Connector Fault

The September 10, 1899 M_w~8.1 thrust earthquake likely promoted failure on the northwest Fairweather Fault (Figure 7), and in turn the 1958 FWF earthquake likely promoted failure on nearby thrust faults of the St. Elias (Figure 9b). Positive feedback loops like these may be characteristic of earthquake interactions in this tectonic corner over the long term and, if so, may assist in the transfer of stress between the FWF and St. Elias. Bufe and Boyd (2008) found a similar feedback loop between the 1958 rupture, the great 1964 M_w = 9.2 subduction earthquake to the west, and the 2002 Denali earthquake to the northwest. We note also that the 1958 earthquake likely inhibited Coulomb failure on the postulated Connector Fault (Figure S7f). While the September 10, 1899 earthquake likely promoted failure on the southernmost Connector Fault (the Art Lewis Glacier Fault), it would have also inhibited failure on it north of ~60° N (Figures 7, S11–S13). This may have contributed to the Connector Fault's relative seismic quiescence over the instrumental period (Figure 1a), and if the 1958 and 1899 earthquakes are characteristic of typical FWF and great St. Elias events, these stress shadow effects would complicate the transfer of tectonic strain from the FWF to the Connector Fault over the long term.

6. Conclusion

We find that GIA driven by rapid 19th-century ice loss in Glacier Bay promoted Coulomb failure at the eventual epicenter of the 1958 M_w~7.8 Fairweather Fault earthquake (Figure 5, Section 4.1), favoring the epicenter for failure and perhaps affecting the earthquake's timing and/or characteristics. Regionwide GIA driven by recent ice loss promoted Coulomb failure at the sites of at least 23 of 30 known $M_w \geq 5.0$ earthquakes in southeast Alaska (Figure 10). While rapid tectonic loading is very likely the main driver of fault stress and earthquakes in this region, our findings suggest that GIA may also impact them. This is consistent with the findings of Sauber and Molnia (2004) and Sauber and Ruppert (2008) that ice load can influence seismicity on seasonal and interannual timescales in the St. Elias. The possible influence of GIA on strike-

Printed by [Nasa Goddard Space Flight - 156.068.119.100 - /doi/epdf/10.1029/2020JB020411] at [16/08/2021].

slip earthquakes on the Queen Charlotte-Fairweather Fault complements the cases of GIA's influence on dip-slip earthquakes in the literature. The 1958 earthquake and other events may have also been favored by static stress transfer from preceding earthquakes (Figures 7–9). These two processes may thus play non-negligible roles in earthquake occurrence in southeast Alaska and perhaps in similar settings elsewhere.

Data Availability Statement

GPS data are provided in Hu and Freymueller (2019).

Acknowledgments
We thank Yan Hu for assistance with the HF19 model, Diane Doser for guidance on the 1958 earthquake slip model, Christopher Johnson for providing the seismic catalog used in Johnson et al. (2020), Lisa Piechocki and Elizabeth McElroy for administrative assistance, and Rob Witter, an anonymous reviewer and many colleagues for insightful feedback that greatly improved this study. Funding was provided by NASA ROSES grant NNX16AK84G.

References

Adams, J. (1989). Postglacial faulting in eastern Canada: Nature, origin and seismic hazard implications. *Tectonophysics*, *163*(3–4), 323–331.
Amos, C. B., Audet, P., Hammond, W. C., Bürgmann, R., Johanson, I. A., & Blewitt, G. (2014). Uplift and seismicity driven by groundwater depletion in central California. *Nature*, *509*(7501), 483–486.
Barbot, S., & Fialko, Y. (2010). A unified continuum representation of post-seismic relaxation mechanisms: Semi-analytic models of afterslip, poroelastic rebound and viscoelastic flow. *Geophysical Journal International*, *182*(3), 1124–1140.
Barbot, S., & Fialko, Y. (2010). Fourier-domain Green's function for an elastic semi-infinite solid under gravity, with applications to earthquake and volcano deformation. *Geophysical Journal International*, *182*(2), 568–582.
Ben-Zion, Y. (2001). Dynamic ruptures in recent models of earthquake faults. *Journal of the Mechanics and Physics of Solids*, *49*(9), 2209–2244.
Berthier, E., Schiefer, E., Clarke, G. K., Menounos, B., & Rémy, F. (2010). Contribution of Alaskan glaciers to sea-level rise derived from satellite imagery. *Nature Geoscience*, *3*(2), 92–95.
Brothers, D. S., Elliott, J. L., Conrad, J. E., Haeussler, P. J., & Kluesner, J. W. (2018). Strain partitioning in southeastern Alaska: Is the Chatham Strait fault active? *Earth and Planetary Science Letters*, *481*, 362–371.
Brothers, D., Kilb, D., Luttrell, K., Driscoll, N., & Kent, G. (2011). Loading of the San Andreas fault by flood-induced rupture of faults beneath the Salton sea. *Nature Geoscience*, *4*(7), 486–492.
Brothers, D. S., Miller, N. C., Barrie, J. V., Haeussler, P. J., Greene, H. G., Andrews, B. D., et al. (2020). Plate boundary localization, slip-rates and rupture segmentation of the Queen Charlotte Fault based on submarine tectonic geomorphology. *Earth and Planetary Science Letters*, *530*, 115882.
Bruhn, R. L., Pavlis, T. L., Plafker, G., & Serpa, L. (2004). Deformation during terrane accretion in the Saint Elias orogen, Alaska. *Geological Society of America Bulletin*, *116*(7–8), 771–787.
Bufe, C. G., & Boyd, O. S. (2008). Fault interaction in Alaska: Static Coulomb stress transfer. *American Geophysical Union Geophysical Monograph Series*, *179*, 417–430. https://doi.org/10.1029/179GM24
Calais, E., Freed, A., Van Arsdale, R., & Stein, S. (2010). Triggering of New Madrid seismicity by late-Pleistocene erosion. *Nature*, *466*(7306), 608–611.
Chinn, T., Fitzharris, B., Willsman, A., & Salinger, M. (2012). Annual ice volume changes 1976–2008 for the New Zealand Southern Alps. *Global and Planetary Change*, *92*, 105–118.
Christeson, G. L., Gulick, S. P., van Avendonk, H. J., Worthington, L. L., Reece, R. S., & Pavlis, T. L. (2010). The Yakutat terrane: Dramatic change in crustal thickness across the Transition fault, Alaska. *Geology*, *38*(10), 895–898.
Colpron, M., Nelson, J., & Murphy, D. C. (2007). Northern Cordilleran terranes and their interactions through time. *Geological Society of America Today*, *17*(4/5), 4.
Craig, T. J., Chanard, K., & Calais, E. (2017). Hydrologically-driven crustal stresses and seismicity in the New Madrid Seismic zone. *Nature Communications*, *8*(1), 1–11.
DeMets, C., Gordon, R. G., & Argus, D. F. (2010). Geologically current plate motions. *Geophysical Journal International*, *181*(1), 1–80.
Dietrich, R., Ivins, E., Casassa, G., Lange, H., Wendt, J., & Fritsche, M. (2010). Rapid crustal uplift in Patagonia due to enhanced ice loss. *Earth and Planetary Science Letters*, *289*(1–2), 22–29.
Ding, K., Freymueller, J. T., Wang, Q., & Zou, R. (2015). Coseismic and early postseismic deformation of the 5 January 2013 M w 7.5 Craig earthquake from static and kinematic GPS solutions. *Bulletin of the Seismological Society of America*, *105*(2B), 1153–1164.
Doser, D. I. (2006). Relocations of earthquakes (1899–1917) in south-central Alaska. *Pure and Applied Geophysics*, *163*(8), 1461–1476.
Doser, D. I. (2010). A reevaluation of the 1958 Fairweather, Alaska, earthquake sequence. *Bulletin of the Seismological Society of America*, *100*(4), 1792–1799.
Doser, D. I. (2014). Seismicity of Southwestern Yukon, Canada, and its relation to slip transfer between the Fairweather and Denali fault systems. *Tectonophysics*, *611*, 121–129.
Doser, D. I., & Lomas, R. (2000). The transition from strike–slip to oblique subduction in southeastern Alaska from seismological studies. *Tectonophysics*, *316*(1–2), 45–65.
Elliott, J., & Freymueller, J. T. (2020). A block model of present-day kinematics of Alaska and western Canada. *Journal of Geophysical Research: Solid Earth*, *125*(7). https://doi.org/10.1029/2019jb018378
Elliott, J., Freymueller, J. T., & Larsen, C. F. (2013). Active tectonics of the St. Elias orogen, Alaska, observed with GPS measurements. *Journal of Geophysical Research: Solid Earth*, *118*(10), 5625–5642. https://doi.org/10.1002/jgrb.50341
Elliott, J. L., Larsen, C. F., Freymueller, J. T., & Motyka, R. J. (2010). Tectonic block motion and glacial isostatic adjustment in southeast Alaska and adjacent Canada constrained by GPS measurements. *Journal of Geophysical Research*, *115*(B9). https://doi.org/10.1029/2009jb007139
Estabrook, C. H., Nábělek, J. L., & Lerner-Lam, A. L. (1992). Tectonic model of the Pacific-North American plate boundary in the Gulf of Alaska from broadband analysis of the 1979 St. Elias, Alaska, earthquake and its aftershocks. *Journal of Geophysical Research*, *97*(B5), 6587–6612.
Firth, C. R., & Stewart, I. S. (2000). Postglacial tectonics of the Scottish glacio-isostatic uplift centre. *Quaternary Science Reviews*, *19*(14–15), 1469–1493.

Printed by [Nasa Goddard Space Flight - 156.068.119.100 - /doi/epdf/10.1029/2020JB020411] at [16/08/2021].

Fradkin, P. L. (2001). *Wildest Alaska: Journeys of great peril in Lituya Bay*. University of California Press.
Grollimund, B., & Zoback, M. D. (2001). Did deglaciation trigger intraplate seismicity in the New Madrid seismic zone? *Geology*, *29*(2), 175–178.
Gulick, S. P., Lowe, L. A., Pavlis, T. L., Gardner, J. V., & Mayer, L. A. (2007). Geophysical insights into the Transition fault debate: Propagating strike slip in response to stalling Yakutat block subduction in the Gulf of Alaska. *Geology*, *35*(8), 763–766.
Hampel, A., & Hetzel, R. (2006). Response of normal faults to glacial-interglacial fluctuations of ice and water masses on Earth's surface. *Journal of Geophysical Research: Solid Earth*, *111*(B6). https://doi.org/10.1029/2005jb004124
Hardebeck, J. L., Nazareth, J. J., & Hauksson, E. (1998). The static stress change triggering model: Constraints from two southern California earthquake sequences. *Journal of Geophysical Research*, *103*, 24427–24437.
Harris, R. A., & Simpson, R. W. (1998). Suppression of large earthquakes by stress shadows: A comparison of Coulomb and rate-and-state failure. *Journal of Geophysical Research: Solid Earth*, *103*(B10), 24439–24451. https://doi.org/10.1029/98jb00793
Heki, K. (2003). Snow load and seasonal variation of earthquake occurrence in Japan. *Earth and Planetary Science Letters*, *207*(1–4), 159–164.
Hetzel, R., & Hampel, A. (2005). Slip rate variations on normal faults during glacial–interglacial changes in surface loads. *Nature*, *435*(7038), 81–84.
Hill, E. M., Davis, J. L., Tamisiea, M. E., Ponte, R. M., & Vinogradova, N. T. (2011). Using a spatially realistic load model to assess impacts of Alaskan glacier ice loss on sea level. *Journal of Geophysical Research*, *116*(B10). https://doi.org/10.1029/2011jb008339
Hu, Y., & Freymueller, J. T. (2019). Geodetic observations of time-variable glacial isostatic adjustment in southeast Alaska and its implications for earth rheology. *Journal of Geophysical Research: Solid Earth*, *124*(9), 9870–9889. https://doi.org/10.1029/2018jb017028
James, T. S., & Bent, A. L. (1994). A comparison of eastern North American seismic strain-rates to glacial rebound strain-rates. *Geophysical Research Letters*, *21*(19), 2127–2130.
Johnson, C. W., Fu, Y., & Bürgmann, R. (2017). Seasonal water storage, stress modulation, and California seismicity. *Science*, *356*(6343), 1161–1164.
Johnson, C. W., Fu, Y., & Bürgmann, R. (2020). Hydrospheric modulation of stress and seismicity on shallow faults in southern Alaska. *Earth and Planetary Science Letters*, *530*, 115904.
Johnston, P., Wu, P., & Lambeck, K. (1998). Dependence of horizontal stress magnitude on load dimension in glacial rebound models. *Geophysical Journal International*, *132*(1), 41–60.
Kalbas, J. L., A. M. Freed, and K. D. Ridgway (2008). Contemporary fault mechanics in southern Alaska. *American Geophysical Union Geophysical Monograph Series*, *179*, 321–336. https://doi.org/10.1029/179GM18
King, G. C., Stein, R. S., & Lin, J. (1994). Static stress changes and the triggering of earthquakes. *Bulletin of the Seismological Society of America*, *84*(3), 935–953.
Koehler, R. D. (2013). *Quaternary faults and folds (QFF): Alaska division of geological & geophysical surveys digital data series 3*. Alaska Division of Geological & Geophysical Surveys. http://doi.org/10.14509/24956
Koehler, R., & Carver, G. (2018). *Active faults and seismic hazards in Alaska. Alaska division of geological & geophysical surveys digital data series 3*. Miscellaneous Publication 160.
Kraner, M. L., Holt, W. E., & Borsa, A. A. (2018). Seasonal nontectonic loading inferred from cGPS as a potential trigger for the M6.0 South Napa earthquake. *Journal of Geophysical Research: Solid Earth*, *123*(6), 5300–5322. https://doi.org/10.1029/2017jb015420
Kreemer, C., & Holt, W. E. (2000). What caused the March 25, 1998 Antarctic plate earthquake?: Inferences from regional stress and strain rate fields. *Geophysical Research Letters*, *27*(15), 2297–2300.
Larsen, C. F., Motyka, R. J., Freymueller, J. T., Echelmeyer, K. A., & Ivins, E. R. (2004). Rapid uplift of southern Alaska caused by recent ice loss. *Geophysical Journal International*, *158*(3), 1118–1133.
Larsen, C. F., Motyka, R. J., Freymueller, J. T., Echelmeyer, K. A., & Ivins, E. R. (2005). Rapid viscoelastic uplift in southeast Alaska caused by post-Little Ice Age glacial retreat. *Earth and Planetary Science Letters*, *237*(3–4), 548–560.
Lay, T., Ye, L., Kanamori, H., Yamazaki, Y., Cheung, K. F., Kwong, K., & Koper, K. D. (2013). The October 28, 2012 Mw 7.8 Haida Gwaii underthrusting earthquake and tsunami: Slip partitioning along the Queen Charlotte fault transpressional plate boundary. *Earth and Planetary Science Letters*, *375*, 57–70.
Luttrell, K., & Sandwell, D. (2010). Ocean loading effects on stress at near shore plate boundary fault systems. *Journal of Geophysical Research*, *115*(B8). https://doi.org/10.1029/2009jb006541
Luttrell, K., Sandwell, D., Smith-Konter, B., Bills, B., & Bock, Y. (2007). Modulation of the earthquake cycle at the southern San Andreas fault by lake loading. *Journal of Geophysical Research*, *112*(B8). https://doi.org/10.1029/2006jb004752
McAleer, R. J., Spotila, J. A., Enkelmann, E., & Berger, A. L. (2009). Exhumation along the Fairweather fault, southeastern Alaska, based on low-temperature thermochronometry. *Tectonics*, *28*(1). https://doi.org/10.1029/2007tc002240
Miller, D. J. (1961). *Giant waves in Lituya Bay, Alaska. United States geological survey professional paper 354-C*. United States Geological Survey.
Morozov, I. B., Smithson, S. B., Chen, J., & Hollister, L. S. (2001). Generation of new continental crust and terrane accretion in southeastern Alaska and western British Columbia: Constraints from P-and S-wave wide-angle seismic data (ACCRETE). *Tectonophysics*, *341*(1–4), 49–67.
Muir-Wood, R. (2000). Deglaciation seismotectonics: A principal influence on intraplate seismogenesis at high latitudes. *Quaternary Science Reviews*, *19*(14–15), 1399–1411.
Muskett, R. R., Lingle, C. S., Tangborn,W. V., & Rabus, B. T. (2003). Multi-decadal elevation changes on Bagley Ice Valley and Malaspina glacier, Alaska. *Geophysical Research Letters*, *30*(16), 2297–2300. https://doi.org/10.1029/2003GL017707
Neves, M., Cabral, J., Luttrell, K., Figueiredo, P., Rockwell, T., & Sandwell, D. (2015). The effect of sea level changes on fault reactivation potential in Portugal. *Tectonophysics*, *658*, 206–220.
Pavlis, T. L., Picornell, C., Serpa, L., Bruhn, R. L., & Plafker, G. (2004). Tectonic processes during oblique collision: Insights from the St. Elias orogen, northern North American Cordillera. *Tectonics*, *23*(3). https://doi.org/10.1029/2003tc001557
Plafker, G., Hudson, T., Bruns, T., & Rubin, M. (1978). Late Quaternary offsets along the Fairweather fault and crustal plate interactions in southern Alaska. *Canadian Journal of Earth Sciences*, *15*(5), 805–816.
Plafker, G., Moore, J. C., Winkler, G. R., & Berg, H. (1994). Geology of the southern Alaska margin, the geology of Alaska: Boulder, Colorado. *Geological Society of America, Geology of North America*, *1*, 389–449.
Plafker, G., & Thatcher, W. (2008). Geological and geophysical evaluation of the mechanisms of the great 1899 Yakutat Bay earthquakes. *American Geophysical Union Geophysical Monograph Series*. *179*, 215–236. https://doi.org/10.1029/179GM12

Printed by [Nasa Goddard Space Flight - 156.068.119.100 - /doi/epdf/10.1029/2020JB020411] at [16/08/2021].

Rice, J. R. (1992). *Fault Stress states, pore pressure distributions, and the weakness of the San Andreas Fault. Fault mechanics and transport properties of rocks*. Academic Press.
Rydelek, P. A., & Sacks, I. S. (1999). Large earthquake occurrence affected by small stress changes. *Bulletin of the Seismological Society of America*, *89*(3), 822–828.
Sato, T., Larsen, C. F., Miura, S., Ohta, Y., Fujimoto, H., Sun, W., et al. (2011). Reevaluation of the viscoelastic and elastic responses to the past and present-day ice changes in Southeast Alaska. *Tectonophysics*, *511*(3–4), 79–88.
Sauber, J., McClusky, S., & King, R. (1997). Relation of ongoing deformation rates to the subduction zone process in southern Alaska. *Geophysical Research Letters*, *24*(22), 2853–2856.
Sauber, J. M., & Molnia, B. F. (2004). Glacier ice mass fluctuations and fault instability in tectonically active Southern Alaska. *Global and Planetary Change*, *42*(1–4), 279–293.
Sauber, J., Plafker, G., Molnia, B. F., & Bryant, M. A. (2000). Crustal deformation associated with glacial fluctuations in the eastern Chugach Mountains, Alaska. *Journal of Geophysical Research*, *105*(B4), 8055–8077.
Sauber, J., & Ruppert, N. A. (2008). Rapid ice mass loss: Does it have an influence on earthquake occurrence in southern Alaska. *Active tectonics and seismic potential of Alaska* (pp. 369–384). Geophysical Monograph Series. https://doi.org/10.1029/179GM21
Schartman, A., Enkelmann, E., Garver, J. I., & Davidson, C. M. (2019). Uplift and exhumation of the Russell Fiord and Boundary blocks along the northern Fairweather transform fault, Alaska. *Lithosphere*, *11*(2), 232–251.
Schell, M. M., & Ruff, L. J. (1989). Rupture of a seismic gap in southeastern Alaska: The 1972 Sitka earthquake (Ms 7.6). *Physics of the Earth and Planetary Interiors*, *54*(3–4), 241–257.
Segou, M., & Parsons, T. (2020). A new technique to calculate earthquake stress transfer and to probe the physics of aftershocks. *Bulletin of the Seismological Society of America*, *110*(2), 863–873. https://doi.org/10.1785/0120190033
Simpson, D., Leith, W., & Scholz, C. (1988). Two types of reservoir-induced seismicity. *Bulletin of the Seismological Society of America*, *78*(6), 2025–2040.
Spada, G., Antonioli, A., Boschi, L., Boschi, L., Brandi, V., Cianetti, S., et al. (2003). Modeling Earth's post-glacial rebound. *Eos, Transactions American Geophysical Union*, *85*(6), 62–64. https://doi.org/10.1029/2004eo060007
Steffen, R., Wu, P., Steffen, H., & Eaton, D. W. (2014). The effect of earth rheology and ice-sheet size on fault slip and magnitude of post-glacial earthquakes. *Earth and Planetary Science Letters*, *388*, 71–80.
Sykes, L. R., Kisslinger, J. B., House, L., Davies, J. N., & Jacob, K. H. (1981). Rupture zones and repeat times of great earthquakes along the Alaska-Aleutian arc, 1784–1980, Earthquake Prediction. *An International Review*, *4*, 73–80.
ten Brink, U. S., Miller, N. C., Andrews, B. D., Brothers, D. S., & Haeussler, P. J. (2018). Deformation of the Pacific/North America plate boundary at Queen Charlotte Fault: The possible role of rheology. *Journal of Geophysical Research: Solid Earth*, *123*(5), 4223–4242. https://doi.org/10.1002/2017jb014770
Tocher, D. (1960). The Alaska earthquake of July 10, 1958: Movement on the Fairweather fault and field investigation of southern epicentral region. *Bulletin of the Seismological Society of America*, *50*(2), 267–292.
Tsuboi, S., Kikuchi, M., Yamanaka, Y., & Kanao, M. (2000). The March 25, 1998 Antarctic earthquake. *Earth Planets and Space*, *52*(2), 133–136.
Wang, K., Hu, Y., Bevis, M., Kendrick, E., Smalley, R., Jr, Vargas, R. B., & Lauría, E. (2007). Crustal motion in the zone of the 1960 Chile earthquake: Detangling earthquake-cycle deformation and forearc-sliver translation. *Geochemistry, Geophysics, Geosystems*, *8*(10). https://doi.org/10.1029/2007gc001721
Weertman, J. (1980). Unstable slippage across a fault that separates elastic media of different elastic constants. *Journal of Geophysical Research*, *85*(B3), 1455–1461.
Working Group on California Earthquake Probabilities (1990). *Probabilities of large earthquakes in the San Francisco bay region*. California: US Geology Survey Circular.
Worthington, L. L., Van Avendonk, H. J., Gulick, S. P., Christeson, G. L., & Pavlis, T. L. (2012). Crustal structure of the Yakutat terrane and the evolution of subduction and collision in southern Alaska. *Journal of Geophysical Research: Solid Earth*, *117*(B1). https://doi.org/10.1029/2011jb008493
Wu, P., & Hasegawa, H. S. (1996). Induced stresses and fault potential in eastern Canada due to a realistic load: A preliminary analysis. *Geophysical Journal International*, *127*(1), 215–229.

References From the Supporting Information

Aagaard, B. T., Knepley, M. G., & Williams, C. A. (2013). A domain decomposition approach to implementing fault slip in finite-element models of quasi-static and dynamic crustal deformation. *Journal of Geophysical Research: Solid Earth*, *118*(6), 3059–3079. https://doi.org/10.1002/jgrb.50217
Detournay, E., & A. H.-D. Cheng (1993), Fundamentals of poroelasticity, In J. A. Hudson & C. Fairhurst (Eds.), *Analysis and design methods* (pp. 113–171). Elsevier.
Dziewonski, A. M., & Anderson, D. L. (1981). Preliminary reference Earth model. *Physics of the Earth and Planetary Interiors*, *25*(4), 297–356.
Kisslinger, J. B. (1983). Some volcanoes, volcanic eruptions, and earthquakes in the former Russian America: Peter Doroshin's account of volcanic activity and earthquakes between 1840 and 1866, the pacific northwest quarterly. *The Pacific Northwest Quarterly*. *74*(2), 59–68.
Melini, D., Gegout, P., Midi–pyrenees, O., & Spada, G. (2015). *REAR - A regional elastic rebound calculator*. Istituto Nazionale di Geofisica e Vulcanologia.
Ochoa Chavez, J. A., & Doser, D. I. (2020). Geophysical analysis of the 30 July 1972 Sitka, Alaska, earthquake sequence. *Geosphere*, *16*(3), 712–722.

Printed by [Nasa Goddard Space Flight - 156.068.119.100 - /doi/epdf/10.1029/2020JB020411] at [16/08/2021].